

## Pressure Enhanced Conductivity in Bis-1,2,3-Thiaselenazoly Dimers

Leanne Beer,<sup>1a</sup> Jaclyn L. Brusso,<sup>1a</sup> Robert C. Haddon,<sup>1b</sup> Mikhail E. Itkis,<sup>1b</sup>  
Holger Kleinke,<sup>1a</sup> Alicea A. Leitch,<sup>1a</sup> Richard T. Oakley,<sup>\*,1a</sup> Robert W. Reed,<sup>1a</sup>  
John F. Richardson,<sup>1c</sup> Richard A. Secco,<sup>1d</sup> and Xueyang Yu<sup>1d</sup>

*Contribution from the Department of Chemistry, University of Waterloo,  
Waterloo, Ontario N2L 3G1, Canada, Department of Chemistry and Center for Nanoscale  
Science and Engineering, University of California, Riverside, California 92521-0403,  
Department of Chemistry, University of Louisville, Louisville, Kentucky 40292, and Department  
of Earth Sciences, University of Western Ontario, London, Ontario N6A 5B7, Canada*

Received July 28, 2005; E-mail: oakley@sciborg.uwaterloo.ca

**Abstract:** A synthetic sequence to salts of N-alkylated pyridine-bridged 1,2,3-thiaselenazolo-1,2,3-thiaselenazolylium cations  $[2]^+$  ( $R_1 = \text{Me}$ , Et;  $R_2 = \text{H}$ ) is described. The corresponding radicals  $2$  ( $R_1 = \text{Me}$ , Et;  $R_2 = \text{H}$ ) can be generated from the cations by chemical or electrochemical reduction. Crystals of the two radicals are isostructural and consist of interpenetrating  $\pi$ -stacked arrays of closed-shell Se–Se  $\sigma$ -bonded dimers  $[2]_2$  laced together with numerous short intermolecular Se–Se, Se–S, and Se–N contacts. Variable-temperature magnetic, conductivity, and near-infrared optical measurements indicate that the bulk materials behave as small band gap semiconductors with room-temperature conductivities  $\sigma_{\text{RT}}$  near  $10^{-6} \text{ S cm}^{-1}$  and thermal activation energies  $E_a$  of 0.32 eV ( $R_1 = \text{Me}$ ) and 0.36 eV ( $R_1 = \text{Et}$ ). LMTO band structure calculations on both compounds are consistent with this interpretation. The application of external pressure leads to dramatic increases in conductivity; at 4 GPa  $\sigma_{\text{RT}}$  reaches a value near  $10^{-1} \text{ S cm}^{-1}$  for  $R_1 = \text{Me}$  and  $10^{-2} \text{ S/cm}$  for  $R_1 = \text{Et}$ . The conductivity remains activated for both compounds, but for  $R_1 = \text{Me}$  the activation energy  $E_a$  is reduced to near 0.03 eV at 5 GPa, suggestive of a weakly metallic state.

### Introduction

The development of electrically conductive organic materials has relied almost exclusively on the use of charge transfer (CT) as the means of generating charge carriers.<sup>2</sup> Over the last 30 years a vast array of conductive CT salts based on tetrathiafulvalene (TTF) donors and/or tetracyanoquinodimethane (TCNQ) acceptors has been prepared and characterized.<sup>3</sup> All of these materials contain two components, i.e., a donor and an acceptor, although recently, single component organic metals have been made by incorporating donor and acceptor moieties into the same molecule and fine-tuning the resulting HOMO–LUMO gap.<sup>4</sup>

For some time we have pursued a different paradigm for conductivity in molecular solids, one based on the idea that a

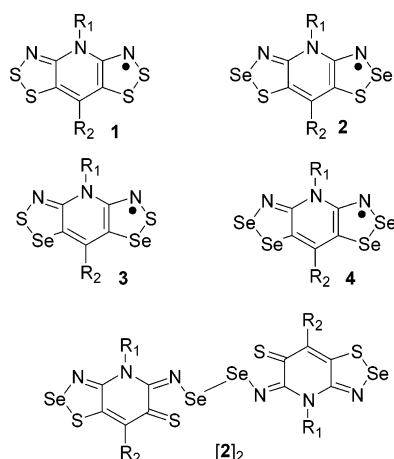
stacked array of  $\pi$ -radicals, each with one unpaired electron, can form the basis for a half-filled energy band and hence afford a metallic ground state.<sup>5</sup> While the tendency of such materials to undergo a charge density wave driven or Peierls distortion<sup>6</sup> (i.e., to dimerize) is ubiquitous, a potentially more serious problem is the high on-site Coulombic repulsion energy  $U$  associated with a half-filled energy band. This feature, coupled with the limited intermolecular overlap and resulting low bandwidth  $W$  intrinsic to all molecular materials, leads to a Mott insulating state.<sup>7</sup> Essentially the spins are trapped on the radicals, and charge transport is suppressed. The challenge has therefore been to design materials with an improved  $W/U$  ratio, i.e., systems with a large bandwidth and a low on-site Coulombic repulsion energy.

In the pursuit of radicals exhibiting high  $W/U$  ratios we recently described the synthesis, structures and transport properties of a series of resonance stabilized bis-1,2,3-dithiazolyl radicals **1** (Chart 1).<sup>8–10</sup> While the a priori estimation of the magnitude of  $U$  for these systems was not practical, the (computed)

- (1) (a) University of Waterloo. (b) University of California. (c) University of Louisville. (d) University of Western Ontario.
- (2) (a) Garito, A. F.; Heeger, A. J. *Acc. Chem. Res.* **1974**, *7*, 232. (b) Torrance, J. B. *Acc. Chem. Res.* **1979**, *12*, 79.
- (3) For recent reviews on CT conductors, see (a) Bendikov, M.; Wudl, F.; Perepichka, D. F. *Chem. Rev.* **2004**, *104*, 4891. (b) Jérôme, D. *Chem. Rev.* **2004**, *104*, 5565. (c) Geiser, U.; Schlueter, J. A. *Chem. Rev.* **2004**, *104*, 5203. (d) Yamada, J.; Akutsu, H.; Nishikawa, H.; Kikuchi, K. *Chem. Rev.* **2004**, *104*, 5057.
- (4) (a) Kobayashi, A.; Fujiwara, E.; Kobayashi, H. *Chem. Rev.* **2004**, *104*, 5243. (b) Kobayashi, H.; Okano, K.; Fujiwara, H.; Tanaka, H.; Tokumoto, M.; Suzuki, W.; Fujiwara, E.; Kobayashi, A. *Proceedings of the NATO Advanced Study Institute on Organic Conductors, Superconductors and Magnets: From Synthesis to Molecular Electronics*, Eds. L. Ouahab and E. Yagubskii, Kluwer Academic Publishers: 2004, pps 81–98.

- (5) (a) Haddon, R. C. *Nature*, **1975**, *256*, 394. (b) Haddon, R. C. *Aust. J. Chem.* **1975**, *28*, 2333. (c) Haddon, R. C. *Aust. J. Chem.* **1975**, *28*, 2334.
- (6) Peierls, R. C. *Quantum Theory of Solids*, Oxford University Press: London, 1955; p. 108.
- (7) Mott, N. F. *Metal–insulator Transitions*, Taylor and Francis, London, 1990.
- (8) Beer, L.; Brusso, J. L.; Cordes, A. W.; Haddon, R. C.; Itkis, M. E.; Kirschbaum, K.; MacGregor, D. S.; Oakley, R. T.; Pinkerton, A. A.; Reed, R. W. *J. Am. Chem. Soc.* **2002**, *124*, 9498.

Chart 1



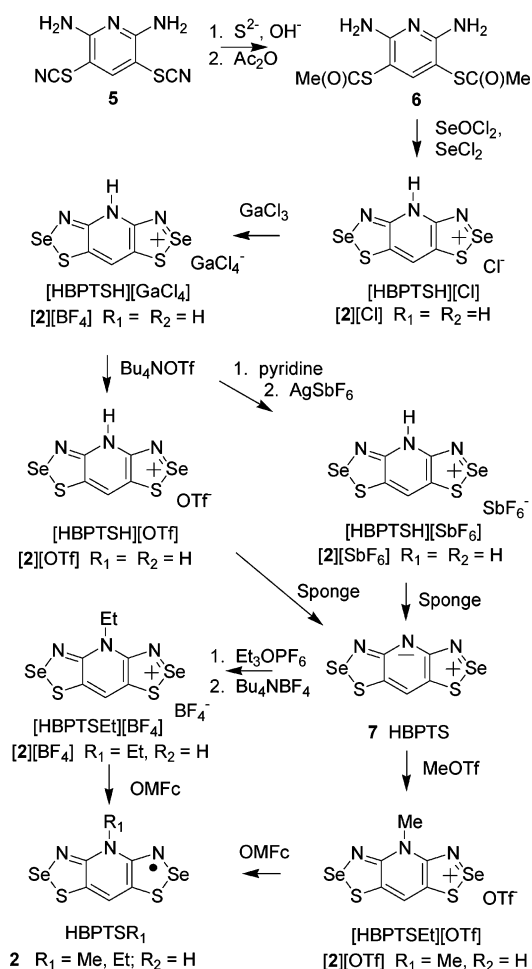
gas-phase disproportionation enthalpies  $\Delta H_{\text{disp}}$  and experimentally measured solution cell potentials,  $E_{\text{cell}}$ , were consistent with a much lower value of  $U$  in the solid state.<sup>11</sup> However, while these materials displayed improved charge transport properties, with values of  $\sigma_{\text{RT}}$  generally near  $10^{-5} \text{ S cm}^{-1}$ , the conductivity remained activated, indicative of the fact that the electronic bandwidth  $W$  arising from the interacting radicals was still insufficient to overcome the on-site Coulombic repulsion  $U$ , so that a Mott insulator ground-state prevailed. Variations in the  $R_1/R_2$  substituents provided some flexibility in crystal packing and hence bandwidth, but computed (extended Hückel) values of  $W$  were generally less than 0.5 eV.

In an attempt to address this bandwidth deficiency we have sought to explore the effects on structure and transport properties of the replacement of sulfur by selenium, a design approach recognized early on in the development of CT salts.<sup>12</sup> In principle there are three possible selenium-containing variants for the bis-dithiazolyl framework 1, i.e., 2, 3, and 4, and in this contribution we describe the preparation and characterization of the first examples of 2 ( $R_1 = \text{Me, Et; } R_2 = \text{H}$ ), both of which associate in the solid state as Se–Se  $\sigma$ -bonded dimers  $[2]_2$  ( $R_1 = \text{Me, Et; } R_2 = \text{H}$ ).<sup>13</sup> The electronic structures of these dimers have been probed at the molecular level by DFT calculations and in the solid state by LMTO methods. Variable-temperature magnetic, conductivity, and optical property measurements indicate that they behave as small band gap semiconductors. Both compounds undergo dramatic conductivity enhancements under relatively mild applied pressures ( $<5 \text{ GPa}$ ).

## Results and Discussion

**Synthesis.** There are only a few reports of methods to replace sulfur by selenium in a 1,2,3-dithiazole ring. The conversion

Scheme 1



of benzo-1,2,3-dithiazolium salts to the corresponding 1,2,3-thiaselenazolium salts in the presence of  $\text{SeO}_2$  has been described,<sup>14</sup> but a more common route is the reaction of an aromatic aminothiols with  $\text{SeCl}_4$ .<sup>15</sup> However, in our hands all attempts to generate  $[2][\text{Cl}]$  ( $R_1 = R_2 = \text{H}$ ) by the condensation of 2,6-diaminopyridine-3,5-dithiol with  $\text{SeCl}_4$  or  $\text{SeOCl}_2$  failed. Success was eventually achieved through the use of the corresponding bis-thioacetate 6 (Scheme 1).

This reagent is more tractable than the corresponding dithiol and can be easily made by quenching the intermediate dithiolate (prepared by the hydrolysis of the bis-thiocyanate 5) with acetic anhydride. More importantly, the acetyl groups of 6 can be easily removed under mild electrophilic conditions to allow the introduction of selenium. We have tested the use of 6 with a wide variety of reagents (e.g.,  $\text{SeCl}_4$ ,  $\text{SeOCl}_2$  and  $\text{SeCl}_2$ ) and reaction conditions, and the best results were obtained by mixing 6 with a mixture of 2 mol equiv of both  $\text{SeOCl}_2$  and  $\text{SeCl}_2$  in the presence of triethylamine. The resulting blue/black precipitate of crude  $[2][\text{Cl}]$  ( $R_1 = R_2 = \text{H}$ ) was converted into a more soluble tetrachlorogallate, from which the purified chloride could be reprecipitated by treatment with pyridine. The purified chloride was then metathesized with  $\text{AgSbF}_6$  to the corresponding hexafluoroantimonate salt  $[2][\text{SbF}_6]$  ( $R_1 = R_2 = \text{H}$ ). Alternatively, a triflate salt  $[2][\text{OTf}]$  ( $R_1 = R_2 = \text{H}$ ) could be

- (9) Beer, L.; Britten, J. F.; Brusso, J. L.; Cordes, A. W.; Haddon, R. C.; Itkis, M. E.; MacGregor, D. S.; Oakley, R. T.; Reed, R. W.; Robertson, C. M. *J. Am. Chem. Soc.* **2003**, *125*, 14394.
- (10) Beer, L.; Britten, J. F.; Clements, O. P.; Haddon, R. C.; Itkis, M. E.; Matkovich, K. M.; Oakley, R. T.; Reed, R. W. *Chem. Mat.* **2004**, *16*, 1564.
- (11)  $H_{\text{disp}}$  is the enthalpy change for the conversion of two gas-phase radicals  $R$  into a cation/anion pair, i.e.,  $2 R \rightleftharpoons R^+ + R^-$ , and is equal to the difference between the ionization potential ( $IP$ ) and electron affinity ( $EA$ ). The cell potential  $E_{\text{cell}} = E_{1/2}(\text{ox}) - E_{1/2}(\text{red})$  is the difference between the half-wave potentials for the oxidation and reduction processes.
- (12) (a) Beechgaard, K.; Cowan, D. O.; Bloch, A. N. *J. Chem. Soc. Chem. Commun.* **1974**, 937. (b) Engler, E. M.; Patel, V. V. *J. Am. Chem. Soc.* **1974**, *96*, 7376.
- (13) A preliminary communication on part of this work has been reported. See Beer, L.; Brusso, J. L.; Haddon, R. C.; Itkis, M. E.; Leitch, A. A.; Oakley, R. T.; Reed, R. W.; Richardson, J. F. *Chem. Commun.* **2005**, 1543.

- (14) Akulin, Yu. I.; Gel'mont, M. M.; Strelets, B. Kh.; Efros, L. S. *Khimiya Geterotsiklicheskikh Soedinenii*, **1978**, 912.
- (15) Oakley, R. T.; Reed, R. W.; Richardson, J. F.; Robertson, C. M. *Inorg. Chem.* **2005**, *44*, 1837.

**Table 1.** Computed  $IP$ ,  $EA$ , and  $\Delta H_{\text{disp}}$  Values (in eV),<sup>a</sup> Selected Spin Densities  $\rho$ , and Hyperfine Coupling Constants  $a$  (in mT)<sup>b</sup>

	compounds			
	1	2	3	4
$IP$	6.16	6.07	6.08	5.99
$EA$	1.39	1.41	1.42	1.45
$\Delta H_{\text{disp}}$	4.77	4.65	4.66	4.54
$\rho_{\text{N(E)}}$	0.175	0.175	0.167	0.167
$\rho_{\text{E(N)}}$	0.092	0.086	0.092	0.088
$\rho_{\text{E(C)}}$	0.125	0.123	0.126	0.125
$a_{\text{N(2N)}}$	0.357	0.342	0.343	0.327
$a_{\text{N(1N)}}$	−0.069	−0.064	−0.066	−0.063
$a_{\text{H(HN)}}$	0.058	0.049	0.057	0.049
$a_{\text{H(HC)}}$	0.356	0.351	0.342	0.331

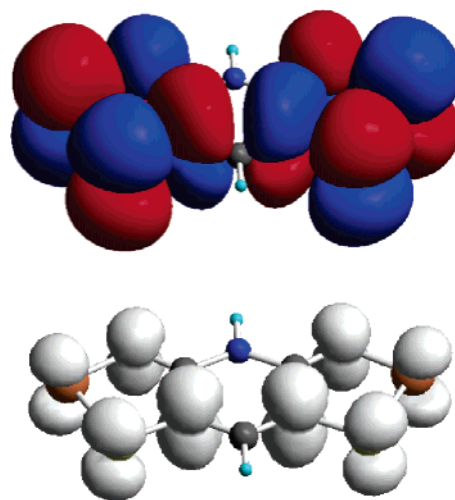
<sup>a</sup>  $\Delta$ SCF values from B3LYP/6-31G\*\* calculations performed within a  $C_{2v}$  symmetry constraint. <sup>b</sup> B3LYP/6-31G\*\* values from a  $C_{2v}$  geometry optimization.

precipitated by the addition of *n*-Bu<sub>4</sub>NOTf to solutions of the gallate in MeCN.

Starting from either the SbF<sub>6</sub><sup>−</sup> or OTf<sup>−</sup> salts, the protonated cation [2]<sup>+</sup> ( $R_1 = R_2 = \text{H}$ ) was converted into the (highly insoluble) zwitterion **7** by treatment with Proton Sponge. Methylation of the latter with methyl triflate in DCE in the presence of Proton Sponge afforded the *N*-methyl salt [2][OTf] ( $R_1 = \text{Me}$ ,  $R_2 = \text{H}$ ). The corresponding *N*-ethyl salt could not be prepared from ethyl triflate and **7**, but ethylation was eventually achieved with triethyloxonium hexafluorophosphate (and Proton Sponge) in DCE. Subsequent metathesis of (deep blue/green) solutions of the crude PF<sub>6</sub><sup>−</sup> salt in THF with *n*-Bu<sub>4</sub>NBF<sub>4</sub> led to the precipitation of lustrous, deep-red microcrystals of the corresponding BF<sub>4</sub><sup>−</sup> salt, i.e., [2][BF<sub>4</sub>] ( $R_1 = \text{Et}$ ,  $R_2 = \text{H}$ ). Final reduction of these salts to the desired radical **2** ( $R_1 = \text{Me}$ , Et;  $R_2 = \text{H}$ ) could be effected using either decamethylferrocene (DMFc) or octamethylferrocene (OMFc). The products were obtained as microcrystalline solids in essentially quantitative yields when the two reagents were brought together in MeCN. Lustrous, gold/bronze crystals of the dimers [2]<sub>2</sub> suitable for X-ray work required slow diffusion of separate solutions of the salt and reductant (OMFc) using H-cell techniques.

**Ion Energetics and Spin Distributions.** A crucial aspect of neutral radical conductor design is the need to minimize the on-site Coulombic repulsion energy  $U$ . While the value of  $U$  is not easily predicted, it is well established that trends in the gas-phase disproportionation enthalpies  $\Delta H_{\text{disp}}$  for a series of related radicals provide a working mirror to the subsequent trends in  $U$ .<sup>16</sup> To this extent the development of the resonance stabilized framework **1** represented a major improvement, as both its  $\Delta H_{\text{disp}}$  and  $E_{\text{cell}}$  values were markedly reduced compared to those of previously studied materials.<sup>8,9</sup> To probe the effects of sulfur/selenium replacement we have carried out DFT calculations at the B3LYP/6-31G\*\* level on a series of model radicals **1–4** ( $R_1 = R_2 = \text{H}$ ), with a view to establishing trends in gas-phase ionization potentials ( $IP$ ) and electron affinities ( $EA$ ). The results are summarized in Table 1.

As noted earlier the superior ion energetics of the bis-dithiazoyl framework **1** can be attributed, in valence bond parlance, to resonance between the two 1,2,3-dithiazoyl rings.<sup>8</sup> Similar reasoning applies to the three selenium-containing

**Figure 1.** B3LYP/6-31G\*\* SOMO for **2** ( $R_1 = R_2 = \text{H}$ ) and derived spin distribution.

variants **2–4**. In molecular orbital terms the extent of spin delocalization is evident in the distribution of the  $a_2$  SOMO illustrated in Figure 1 for **2** ( $R_1 = R_2 = \text{H}$ ); derived total spin densities are also shown. As can be seen from the data in Table 1, the variations in spin distributions occasioned by the replacement of sulfur by selenium along the series **1–4** ( $R_1 = R_2 = \text{H}$ ) are small. The computed spin densities and EPR coupling constants reveal the same minor trends seen elsewhere, i.e., that replacement of sulfur in thiazyl radicals by selenium leads to a slight polarization of spin density away from selenium onto the neighboring nitrogen.

From an experimental standpoint we have probed the redox chemistry of **2** ( $R_1 = \text{Me}$ , Et;  $R_2 = \text{H}$ ) by cyclic voltammetry, starting from solutions of the corresponding cations [2]<sup>+</sup> in MeCN. In the case of the sulfur-based radicals **1** a series of waves, corresponding to the  $-1/0$ ,  $0/+1$ , and  $+1/+2$  processes, were observed. The more anodic processes were always reversible, but the reversibility of the  $-1/0$  process required the presence of electron-accepting  $R_2$  substituents. This we attributed to the fragility of the S–S bond in the reduced state, a feature noted also in computational work. Similar problems have been encountered in the selenium-containing materials **2** ( $R_1 = \text{Me}$ , Et;  $R_2 = \text{H}$ ), and were exacerbated by the insolubility of the radicals, which tended to plate out on and poison the working electrode. As a result we are unable to report any potential data for the severely irreversible  $-1/0$  wave. Clean  $0/+1$  waves could, however, be obtained for both  $R_1 = \text{Me}$ , with  $E_{1/2} = -0.097$  V vs SCE, and  $R_1 = \text{Et}$ , with  $E_{1/2} = -0.108$  V vs SCE. These values are slightly more anodic than those observed for the purely sulfur-based compounds.<sup>9</sup>

Attempts to record the solution EPR spectrum of **2** ( $R_1 = \text{Me}$ ,  $R_2 = \text{H}$ ) were precluded by its extremely low solubility in all organic media.<sup>17</sup> Fortunately, the corresponding ethyl compound **2** ( $R_1 = \text{Et}$ ,  $R_2 = \text{H}$ ) was slightly soluble, and we were able to record its spectrum.<sup>13</sup> Although the resolution of the spectrum ( $g = 2.0099$ ) was compromised by spin–orbit broadening resulting from the presence of selenium, we were able to extract the major hyperfine coupling constants by

(16) (a) Kaszynski, P. *J. Phys. Chem. A* **2001**, *105*, 7626. (b) Boeré, R. T.; Roemmele, T. L. *Coord. Chem. Rev.* **2000**, *210*, 369. (c) Kaszynski, P. *J. Phys. Chem. A* **2001**, *105*, 7615. (d) Cordes, A. W.; Haddon, R. C.; Oakley, R. T. *Phosphorus, Sulfur, Silicon and Related Elements* **2004**, *179*, 673.

(17) The absence of an EPR signal may also arise because of the complete association of the radicals in solution to afford diamagnetic dimers [2]<sub>2</sub>, as observed in the solid state.



**Table 2.** Crystallographic Data

	compound		
	[2][OTf] (R <sub>1</sub> = Me, R <sub>2</sub> = H)	[2] <sub>2</sub> (R <sub>1</sub> = Me, R <sub>2</sub> = H)	[2] <sub>2</sub> (R <sub>1</sub> = Et, R <sub>2</sub> = H)
formula	C <sub>7</sub> H <sub>4</sub> F <sub>3</sub> N <sub>3</sub> O <sub>3</sub> S <sub>3</sub> Se <sub>2</sub>	C <sub>12</sub> H <sub>8</sub> N <sub>6</sub> S <sub>4</sub> Se <sub>4</sub>	C <sub>14</sub> H <sub>12</sub> N <sub>6</sub> S <sub>4</sub> Se <sub>4</sub>
fw	489.23	680.32	708.38
a, Å	7.2269(18)	4.924(4)	4.8546(8)
b, Å	8.653(2)	12.616(11)	12.692(2)
c, Å	12.729(3)	15.086(13)	16.472(3)
α, deg	102.354(4)	90	90
β, deg	98.757(4)	94.563(14)	97.624(3)
γ, deg	110.608(4)	90	90
V, Å <sup>3</sup>	704.9(3)	934.1(14)	1005.9(3)
ρ(calcd), g cm <sup>-3</sup>	2.305	2.419	2.339
space group	P1̄	P2 <sub>1</sub> /c	P2 <sub>1</sub> /c
Z	2	2	2
temp, K	295(2)	295(2)	295(2)
μ, mm <sup>-1</sup>	5.734	8.314	7.725
λ, Å	0.71073	0.71073	0.71073
data/restraints/parameters	3501/0/215	2027/0/119	2379/0/1280
solution method	direct methods	direct methods	direct methods
R, R <sub>w</sub> (on F <sup>2</sup> ) <sup>a</sup>	0.0317, 0.0757	0.0439, 0.0939	0.0280, 0.0697

<sup>a</sup>  $R = [\sum ||F_o| - |F_c||] / [\sum |F_o|]$  for  $I > 2 \sigma(I)$ ;  $R_w = \{[\sum w||F_o|^2 - |F_c|^2|^2] / [\sum (w|F_o|^4)]\}^{1/2}$ .

simulation, and the experimental values ( $a_N = 0.30$  mT,  $a_H = 0.30$  mT) were in good agreement with those predicted by calculation (Table 1).

**Crystal Structures.** In contrast to the corresponding all-sulfur compounds **1**, crystals of **2** ( $R_1 = \text{Me}$ ,  $\text{Et}$ ,  $R_2 = \text{H}$ ) suitable for X-ray work could not be grown by recrystallization or sublimation, as the materials were too insoluble and involatile. Electroreduction of the cations **[2]<sup>+</sup>** was likewise ineffective, affording chemically pure, but highly dendritic deposits on the cathode. Slow diffusion of a solution of a **[2]<sup>+</sup>** salt into a solution of reducing agent eventually proved to be the technique of choice, but critical to the success of the approach was the selection of reductant. On the basis of the measured half-wave potentials  $E_{1/2}$  (0/+1) for **[2]<sup>+</sup>** (vide supra) the use of DMFc ( $E_{1/2}$  (0/+1) = −0.13 V vs SCE)<sup>18</sup> seemed logical. However, while very pure **2** could be obtained by diffusion of solutions of **[2]<sup>+</sup>** and DMFc in MeCN, the product was still microcrystalline and highly dendritic. In the belief that improvement in both crystal size and quality could be achieved by slowing the rate of electron-transfer, we explored the use of OMFc ( $E_{1/2}$  (0/+1) = −0.0375 V vs SCE) as the reducing agent.<sup>19</sup> To our satisfaction this modification did indeed allow slower and more controlled crystal growth. Some twinning of the methyl derivative was still present, but complete structural characterization of both compounds was nonetheless possible. Table 2 provides crystal data for **[2][OTf]** ( $R_1 = \text{Me}$ ,  $R_2 = \text{H}$ ) and **[2]<sub>2</sub>** ( $R_1 = \text{Me}$ ,  $\text{Et}$ ;  $R_2 = \text{H}$ ). The former provides a benchmark for the analysis of structural changes as a function of oxidation state. Pertinent intra- and intermolecular distances are summarized in Table 3.

Crystals of **[2][OTf]** ( $R_1 = \text{Me}$ ,  $R_2 = \text{H}$ ) belong to the triclinic space group  $P\bar{1}$ , and consist (Figure 2) of **[2]<sup>+</sup>** cations bridged by triflate anions ( $\text{Se1} \cdots \text{O1}' = 2.855(3)$  Å,  $\text{S1} \cdots \text{O1}' = 3.123(3)$  Å,  $\text{Se2} \cdots \text{O3}' = 2.826(3)$  Å,  $\text{S2} \cdots \text{O3}' = 3.141(3)$

**Table 3.** Intra- and Intermolecular Distances (Å) and Angles (deg) in **[2][OTf]** and **[2]<sub>2</sub>**

	compound		
	[2][OTf] (R <sub>1</sub> = Me, R <sub>2</sub> = H)	[2] <sub>2</sub> (R <sub>1</sub> = Me, R <sub>2</sub> = H)	[2] <sub>2</sub> (R <sub>1</sub> = Et, R <sub>2</sub> = H)
C2–N1	1.299(4)	1.309(8)	1.303(4)
C3–N3	1.301(4)	1.298(7)	1.288(3)
N1–Se1	1.792(2)	1.823(5)	1.818(2)
N3–Se2	1.789(2)	1.816(5)	1.811(2)
C4–S2	1.707(3)	1.694(6)	1.679(3)
C1–S1	1.704(3)	1.726(6)	1.719(3)
Se1–S1	2.1984(10)	2.232(2)	2.2145(9)
Se2–S2	2.1949(10)	2.785(3)	2.7847(9)
Se2–Se2'	—	2.460(2)	2.4628(8)
τ <sup>a</sup>	—	45.89(5)	47.53(2)
δ <sup>b</sup>	—	3.535(2)	3.5811(6)
θ <sup>c</sup>	—	174.4(5)	168.1(2)
Se1–N1' d <sub>1</sub>	3.092(3)	2.892(5)	3.238(3)
Se2–N3' d <sub>2</sub>	2.959(3)	2.984(5)	3.004(3)
S2–S1' d <sub>3</sub>	—	3.268(3)	3.245(1)
S2–Se1' d <sub>4</sub>	—	3.177(2)	3.335(1)
Se2–S1' d <sub>5</sub>	—	3.663(3)	3.966(1)

<sup>a</sup> τ is the tilt angle between the mean molecular plane and the x axis. <sup>b</sup> δ is the interplanar separation of molecules. <sup>c</sup> θ is the C3–N3–Se2–Se2' torsion angle.

Å). At an intramolecular level, the internal bond lengths in the cation are, as expected, similar to those observed in the corresponding cation **[2]<sup>+</sup>** ( $R_1 = R_2 = \text{H}$ )<sup>13</sup> and serve as reference points for the structural features of the reduced materials described below. In addition to ion-pairing contacts neighboring cations are laced together into ribbonlike arrays by close centrosymmetric four-center Se–N' interactions (d<sub>1</sub>, d<sub>2</sub>). These latter interactions, which are ubiquitous in both closed-shell and open-shell selenazoles,<sup>15,20</sup> are stronger<sup>21</sup> than the corresponding S–N contacts and play a major role as structure-making supramolecular synthons.<sup>22</sup> As a result we anticipated their presence in the solid-state structure of the neutral radicals **2** ( $R_1 = \text{Me}$ ,  $\text{Et}$ ;  $R_2 = \text{H}$ ). While this expectation proved to be partially correct, we underestimated the extent and nature of the interaction.

Crystals of **[2]<sub>2</sub>** ( $R_1 = \text{Me}$ ,  $\text{Et}$ ;  $R_2 = \text{H}$ ) are isostructural, both belonging to the monoclinic space group  $P2_1/c$ ; a unit cell drawing for  $R_1 = \text{Me}$  is shown in Figure 3. As expected the molecules adopt a normal slipped π-stacked motif, in which the molecules appear to be linked laterally into ribbons, much as the cations are in the triflate salt above. However, closer inspection of the lateral intermolecular contacts reveals that, while the radicals are coupled at both ends by short 4-center Se1–N1' contacts d<sub>1</sub> and d<sub>2</sub>, they are actually fused at the one end by a covalent Se2–Se2' σ-bond (2.460(2) Å for  $R_1 = \text{Me}$ , 2.4628(8) Å for  $R_1 = \text{Et}$ ). At the same time, the associated Se2–S2 bond opens to a value (2.785(3) Å for  $R_1 = \text{Me}$ , 2.7847(9) Å for  $R_1 = \text{Et}$ ) intermediate between the sum of the covalent radii<sup>23</sup> and the expected van der Waals contact.<sup>24</sup>

(18) Cinquantani, A.; Opromolla, G.; Zanello, P.; Giorgi, G. *J. Organomet. Chem.* **1985**, *89*, 2787.

(19) (a) Zou, C.; Wrighton, M. S. *J. Am. Chem. Soc.* **1990**, *112*, 7578. (b) Miller, J. S.; Glatzhofer, D. T.; O'Hare, D. M.; Reiff, W. M.; Chakraborty, A.; Epstein, A. J. *Inorg. Chem.* **1989**, *28*, 2930. (c) Hobi, M.; Rupert, O.; Gramlich, V.; Togni, A. *Organometallics* **1997**, *16*, 1384. (d) Plenio, H.; Aberle, C. *Organometallics* **1997**, *16*, 5950.

(20) (a) Cordes, A. W.; Haddon, R. C.; Oakley, R. T.; Schneemeyer, L. F.; Waszczak, J. V.; Young, K. M.; Zimmerman, N. M. *J. Am. Chem. Soc.* **1991**, *113*, 582. (b) Cordes, A. W.; Haddon, R. C.; Hicks, R. G.; Oakley, R. T.; Palstra, T. T. M. *Inorg. Chem.* **1992**, *31*, 1802. (c) Beer, L.; Cordes, A. W.; Myles, D. J. T.; Oakley, R. T.; Taylor, N. J. *CrystEngComm* **2000**, *2* (20), 109. (d) Barclay, T. M.; Cordes, A. W.; Goddard, J. D.; Mawhinney, R. C.; Oakley, R. T.; Preuss, K. E.; Reed, R. W. *J. Am. Chem. Soc.* **1997**, *119*, 12136.

(21) Cozzolino, A. F.; Vargas-Baca, I.; Mansour, S.; Mahmoudkhani, A. J. *J. Am. Chem. Soc.* **2005**, *127*, 3184.

(22) (a) Desiraju, G. R. *J. Mol. Struct.* **2003**, *656*, 5. (b) Desiraju, G. R. *Chem. Commun.* **1997**, 1475.

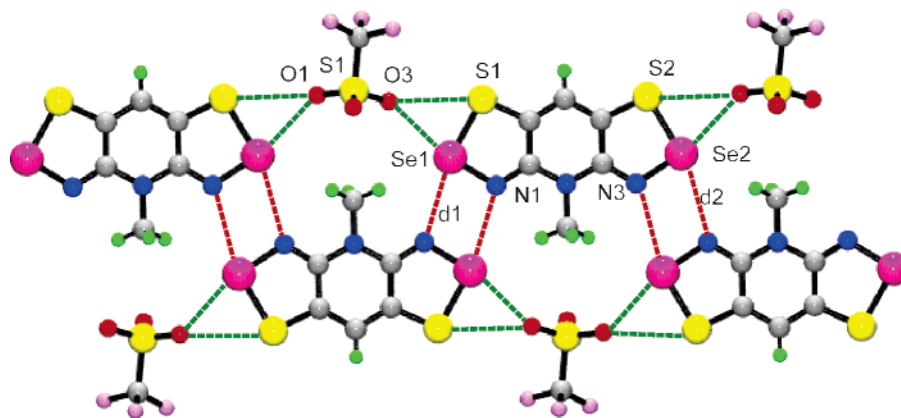


**Figure 2.** Packing of  $[2][\text{OTf}]$  ( $R_1 = \text{Me}$ ,  $R_2 = \text{H}$ ). Intermolecular Se...N' and S/Se...O' contacts are shown with dashed lines.

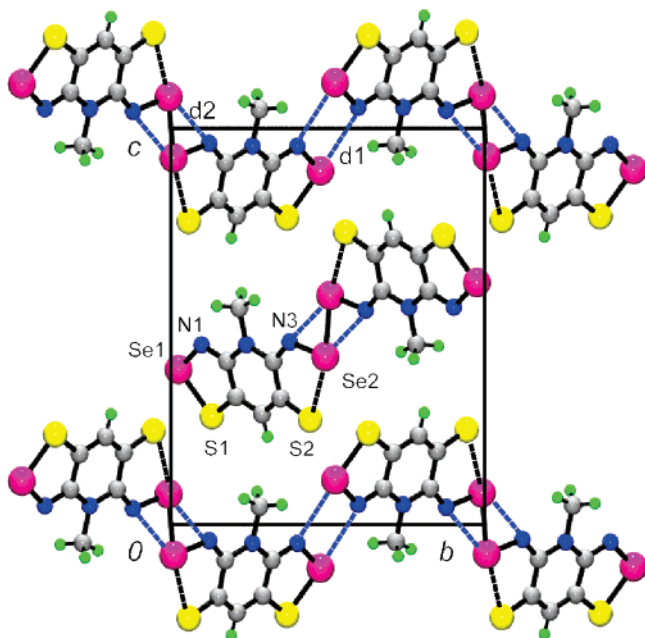


**Figure 3.** Unit cell of  $[2]_2$  ( $R_1 = \text{Me}$ ,  $R_2 = \text{H}$ ), viewed along the  $x$  direction.

Within this dimer or super molecule there is a series of bond length changes relative to those seen in the  $[2]^+$  cation, e.g., a shortening of the C3–N3 and C4–S2 distances (Table 3), all of which are consistent with the closed-shell valence bond formulation  $[2]_2$ . The two halves of each dimer are planar to within 0.160 Å for both  $R_1 = \text{Me}$  and Et, but there is a slight mutual displacement of the two halves by 0.419(2) Å ( $R_1 = \text{Me}$ ) and 0.8495(9) Å ( $R_1 = \text{Et}$ ). This displacement gives rise to a deviation in the value of the C3–N3–Se2–Se2' torsion angle  $\theta$ , which would be 180° if the two halves were rigorously coplanar. For  $R_1 = \text{Me}$ ,  $\theta = 174.4(5)^\circ$  and for  $R_1 = \text{Et}$ ,  $\theta = 168.1(2)^\circ$ .

Dimers within the slipped  $\pi$ -stack arrays (Figure 4) are inclined to the  $x$  axis at angles  $\tau$  of 45.89(5)° for  $R_1 = \text{Me}$  and 47.53(2)° for  $R_1 = \text{Et}$ ; these values are somewhat greater than those found in slipped stack bis-1,2,3-dithiazolyis **1**. The mean interplanar separation ( $\delta$ ) along the stacks, equal to 3.535(2) Å for  $R_1 = \text{Me}$  and 3.5811(6) Å for  $R_1 = \text{Et}$ , is also somewhat larger, as expected by the presence of the larger heteroatom.

The sense of slippage of consecutive  $\pi$ -stacks alternates along the  $z$ -direction, so as to produce a cross-braced arrangement. At the point of intersection of the stacks there is a series of close intermolecular Se...S' and S...S' contacts (d3, d4, and d5 in Table 3), all of which stabilize the S2...Se2–Se2'...S2' sequence.

**Magnetic Susceptibility Measurements.** Variable-temperature magnetic susceptibility  $\chi$  measurements on  $[2]_2$  ( $R_1 = \text{Me}$ , Et;  $R_2 = \text{H}$ ) confirm that both compounds are essentially diamagnetic, i.e., the radicals are spin paired in the dimers. Plots of  $\chi$  (corrected for diamagnetic contributions using Pascal's constants)<sup>25</sup> vs  $T$  for both compounds, shown in Figure 5, reveal a small residual paramagnetism. The low values of  $\chi T$  at 300 K (insets to Figure 5) suggest residual defect spin concentrations of less than 4% ( $R_1 = \text{Me}$ ) and 5% ( $R_1 = \text{Et}$ ). A Curie–Weiss fit to the data above 250 K provides values of  $C = 0.023 \text{ emu mol}^{-1} \text{ K}^{-1}$  and  $\Theta = -163 \text{ K}$  (for  $R_1 = \text{Me}$ ) and  $C = 0.033 \text{ emu mol}^{-1} \text{ K}^{-1}$  and  $\Theta = -197 \text{ K}$  (for  $R_1 = \text{Et}$ ), i.e., the residual spins are strongly antiferromagnetically coupled. This we interpret in terms of pairwise interactions between unassociated radicals.

**Radical Dimerization.** The  $\sigma$ -bonded mode of association for the radicals **2** ( $R_1 = \text{Me}$ , Et;  $R_2 = \text{H}$ ) is, to our knowledge, without precedent. While spin pairing dimerization of selenium-based  $\pi$ -radicals, e.g., diselenadiazolyis **8**, is well-known, the mode of association has, with one exception,<sup>26</sup> involved the cofacial coupling of radical  $\pi$ -SOMOs by a resonance interaction  $\beta$  so as to produce a diamagnetic  $\pi$ -dimer  $[8]_2$  (Figure 6).

To investigate the electronic and energetic changes associated with  $\sigma$ -dimerization we have performed a series of DFT calculations, at the B3LYP/6-31G\*\* level, on model radicals **1–4** ( $R_1 = R_2 = \text{H}$ ) and their respective  $\sigma$ -bonded dimers. The resulting dimer dissociation energies shown in Table 4, i.e., the enthalpy changes for the reaction shown in Scheme 2, indicate that all the dimers save for  $[3]_2$  are stable with respect to the radicals. The preferred combination for maximum dimer stability appears to be that which combines a bridging Se–Se bond with a terminal thione group, as found for **2** ( $R_1 = \text{Me}$ , Et;  $R_2 = \text{H}$ ). We interpret these trends in terms of the well-recognized preference of sulfur at the E<sub>1</sub> position to form a double bond to carbon combined with the ability of selenium at the E<sub>2</sub> posi-

(23) Chen, C. M.; Dojahn, J. G.; Wentworth, W. E. *J. Phys. Chem. A* **1997**, *101*, 3088.

(24) Bondi, A. *J. Phys. Chem.* **1964**, *68*, 441.

(25) Carlin, R. L. *Magnetochemistry*; Springer-Verlag: Berlin, 1986; p 3.

(26) Bryan, C. D.; Cordes, A. W.; Oakley, R. T.; Spence, R. E. *Acta Crystallogr.* **1995**, *C51*, 2402.

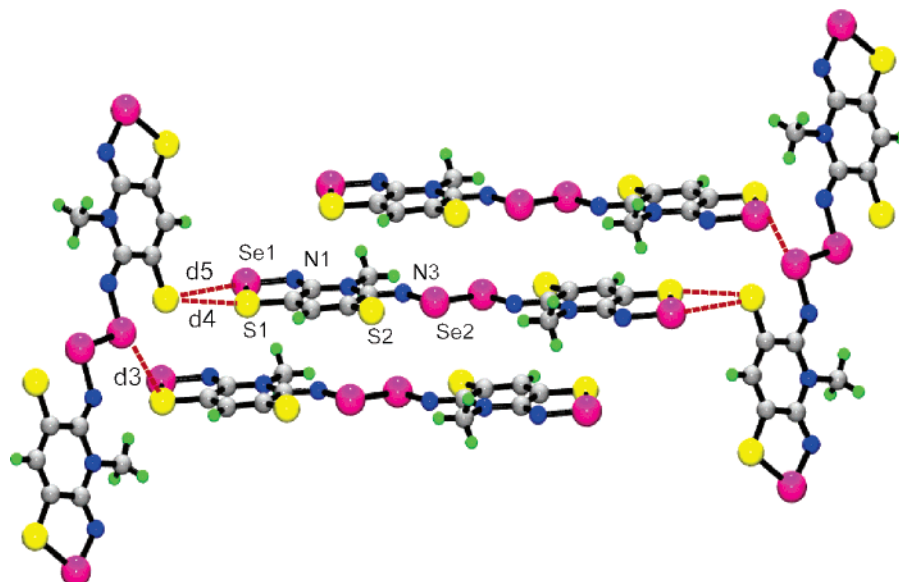


**Figure 4.** Slipped  $\pi$ -stacks of  $[2]_2$  ( $R_1 = \text{Me}$ ,  $R_2 = \text{H}$ ), showing the interstack contacts d3–d5.

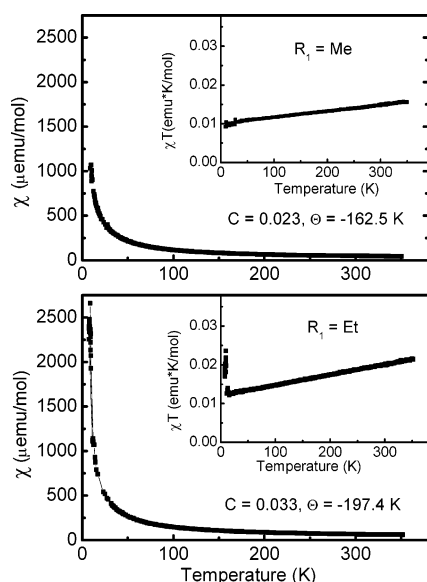


**Figure 5.** Plots of  $\chi$  vs  $T$  for  $[2]_2$  ( $R_1 = \text{Me}$ ,  $\text{Et}$ ;  $R_2 = \text{H}$ ). Insets show plots of  $\chi T$  vs  $T$ .

tion to form a more stable hypervalent  $E_1 \cdots E_2 \cdots E_2 \cdots E_1$  arrangement.

There are important symmetry differences between the standard cofacial  $\pi$ -dimerization (Figure 6) and the  $\sigma$ -dimerization reported here. In essence a configurational change is required to produce a  $\sigma$ -bond. Radicals **1–4** are  $17\pi$ -electron species, but in the dimers the two halves each possess  $18\pi$ -electron counts. Association therefore requires a net  $\sigma \rightarrow \pi$  conversion of one electron per radical. The necessary orbital changes are illustrated in Figure 7, which shows a qualitative FMO correlation diagram for the  $\sigma$ -dimerization process. Both the in-phase and out-of-phase combinations of the radical  $\pi$ -SOMOs (Figure 1) correlate with two occupied levels in the dimer. At the same time, two formerly occupied lone pair  $\sigma$ -orbitals are converted into two new  $\sigma$ -combinations, only one of which, a strongly  $E_2$ – $E_2$  bonding and  $E_1$ – $E_2$  antibonding distribution, remains filled. The net result of this reorganization is that, while the HOMO and LUMO of  $[2]_2$  are still  $\pi$ -type

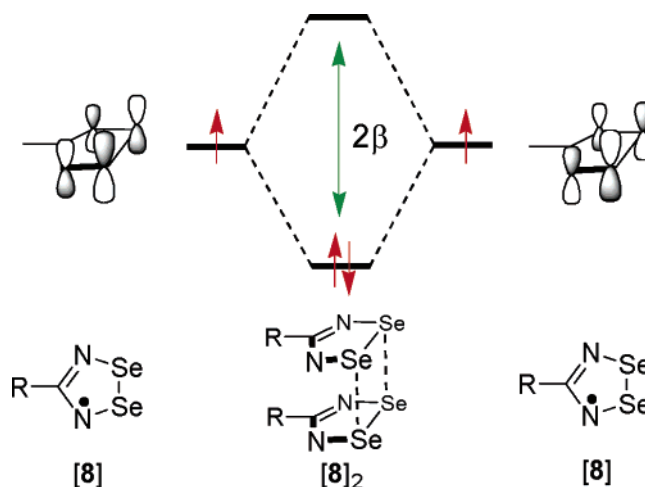


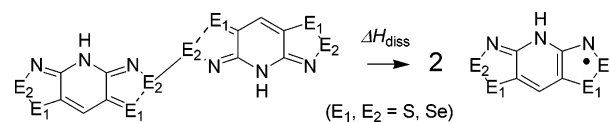
**Figure 6.** Cofacial  $\pi$ -dimerization of diselenadiazolyl radicals.

**Table 4.** B3LYP/6-31G\*\* Dimer Dissociation Enthalpies ( $\text{kcal mol}^{-1}$ ) and Bond Distances ( $\text{\AA}$ )<sup>a</sup>

	$[1]_2$ , SSN	$[2]_2$ , SSeN	$[3]_2$ , SeSN	$[4]_2$ , SeSeN
$\Delta H_{\text{diss}}^b$	11.12	18.19	−1.123	8.87
$E_2$ – $E_2$	2.233	2.475	2.263	2.496
$E_2 \cdots E_1$	2.885	2.892	2.930	2.910
$E_2$ –N	1.662	1.811	1.660	1.811
$C=E_1$	1.674	1.678	1.807	1.812
$C=N$	1.295	1.293	1.297	1.296

<sup>a</sup> Bond distances for the fused rings. <sup>b</sup> For the reaction presented in Scheme 2.

**Scheme 2**



orbitals, they are not in-phase and out-of-phase combinations of  $\pi$ -SOMOs separated by a resonance energy  $2\beta$ , as they are in  $[8]_2$ .<sup>27</sup> The consequences of this electronic difference on the pressure dependence of the conductivity of these two systems ( $[2]_2$  and  $[8]_2$ ) are described below.

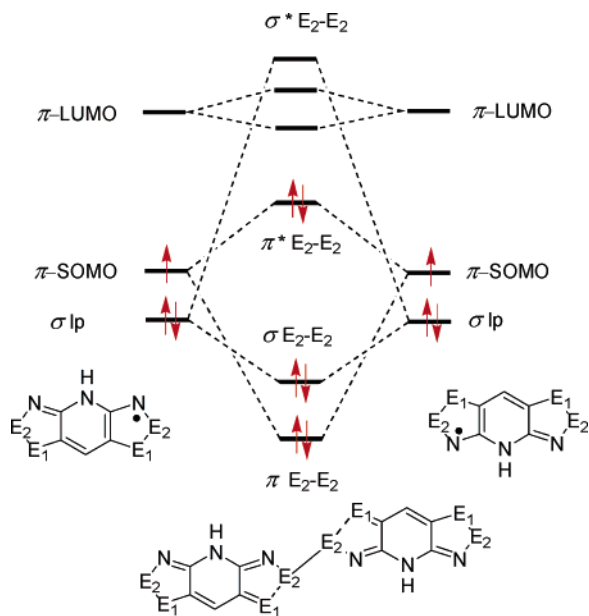


**Figure 7.** Qualitative FMO correlation diagram for the  $\sigma$ -dimerization of radicals **1–4** ( $E_1, E_2 = \text{S, Se}$ ).

**Band Structures.** The DFT calculations above indicate that, at the molecular level, the  $\sigma$ -dimers  $[2]_2$  ( $R_1 = \text{Me, Et}$ ;  $R_2 = \text{H}$ ) are closed-shell species. To probe the electronic structures of the materials in the solid-state we have carried out band structure calculations on the crystal structures of  $[2]_2$ . In previous work we have used extended Hückel theory for this purpose, but in the present systems the method fails to respond to the electronic redistribution effected by the dimerization of the radicals and suggests an open shell structure even for the gas phase dimer. We therefore moved to the use of the LMTO SCF method, where electron correlation is included explicitly, and which has been used successfully to describe the band structures of organic solids.<sup>28</sup>

The results, illustrated in Figure 8 as crystal orbital dispersion curves spanning the principal directions of reciprocal space, support the interpretation that both compounds  $[2]_2$  ( $R_1 = \text{Me, Et}$ ;  $R_2 = \text{H}$ ) are small band gap semiconductors. In accord with the observation that the methyl compound is more tightly packed than the ethyl derivative, the estimated indirect optical band gap  $E_g$  for  $R_1 = \text{Me}$  (0.31 eV) is noticeably lower than for  $R_1 = \text{Et}$  (0.46 eV).

**Near Infrared Spectra.** We have measured the near-infrared spectra of crystalline samples of the two radical dimers  $[2]_2$  ( $R_1 = \text{Me, Et}$ ;  $R_2 = \text{H}$ ). The results are presented in Figure 9, which shows the IR transmittance over the range 650–11000  $\text{cm}^{-1}$ . The absorptions in the mid-IR region between 650 and 3100  $\text{cm}^{-1}$  are due to molecular vibrations of the dimer. In addition, there is in both cases a well-developed, low-lying absorption cutoff which we interpret as corresponding to a valence band to conduction band excitation. The optical energy gaps  $E_g$  have threshold values near 0.25 eV ( $R_1 = \text{Me}$ ) and 0.4 eV ( $R_1 = \text{Et}$ ), increasing to near 0.5 and 0.7 eV, respectively, at the mobility edge. These values are qualitatively in agreement with the values predicted by the LMTO calculations.

(27) At the B3LYP/6-31G\*\* level the three highest occupied orbitals are those shown in Figure 7. The  $\sigma$ -orbital which is the out-of-phase partner to the  $E_1$ – $E_2$  bonding orbital is the LUMO+2. Two  $\pi$ -type virtual orbitals intrude at slightly lower energies. A full listing of orbital energies and distributions is available as Supporting Information.

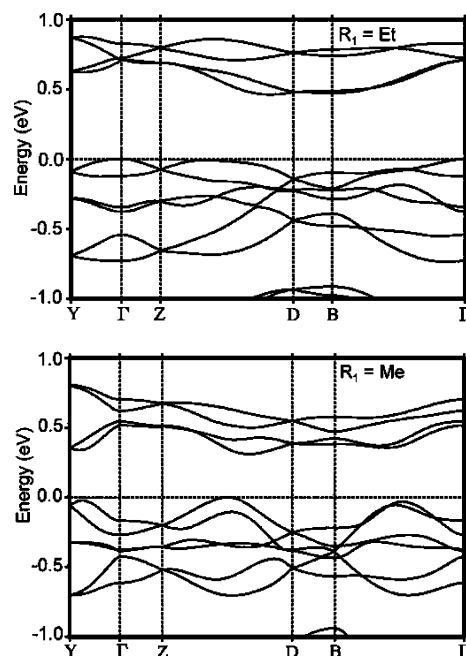


**Figure 8.** LMTO dispersion curves for  $[2]_2$  ( $R_1 = \text{Me, Et}$ ;  $R_2 = \text{H}$ ).

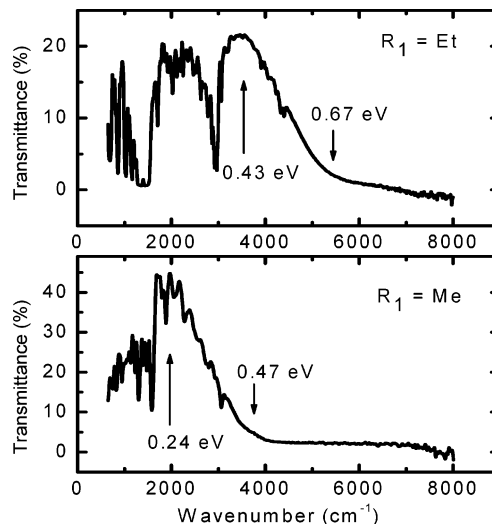


**Figure 9.** Single-crystal IR transmission spectrum of crystalline  $[2]_2$  ( $R_1 = \text{Me, Et}$ ;  $R_2 = \text{H}$ ).

**Conductivity Measurements.** Ambient pressure four-probe variable-temperature conductivity measurements have been performed on both radical dimers  $[2]_2$  ( $R_1 = \text{Me, Et}$ ;  $R_2 = \text{H}$ ). Needles of the ethyl compound were sufficiently large to allow single-crystal measurements, but the smaller crystal dimensions of the methyl derivative precluded such an approach. The data presented in Figure 10 for  $R_1 = \text{Me}$  were therefore obtained from a pressed pellet sample.

The results indicate that conductivity is activated for both compounds, with values of  $\sigma$  (300 K) of  $2.3 \times 10^{-6} \text{ S cm}^{-1}$  ( $R_1 = \text{Me}$ ) and  $5.8 \times 10^{-7} \text{ S cm}^{-1}$  ( $R_1 = \text{Et}$ ) and thermal activation energies  $E_a$  of 0.32 eV ( $R_1 = \text{Me}$ ) and 0.36 eV ( $R_1 = \text{Et}$ ). If the materials are treated as intrinsic semiconductors, these values can be related to the optical band gap  $E_g$  by the expression  $E_a = 1/2 E_g$ . Within the confines of this model, the  $E_g$  values derived from the conductivity data are in reasonable

(28) Sommer-Larsen, P.; Gajhede, M. *Phys. Rev. B* **1992**, *43*, 5119.



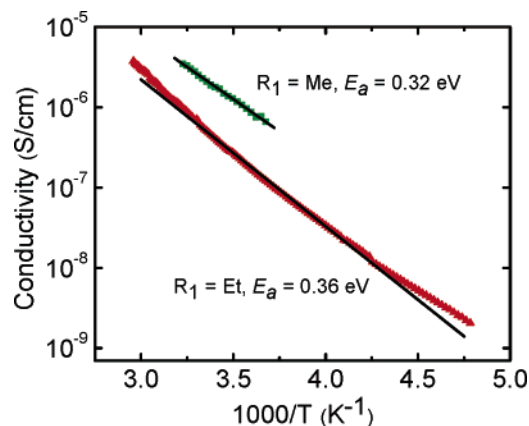


**Figure 10.** Ambient pressure variable temperature conductivities of  $[2]_2$  ( $R_1 = \text{Me}, \text{Et}; R_2 = \text{H}$ ).

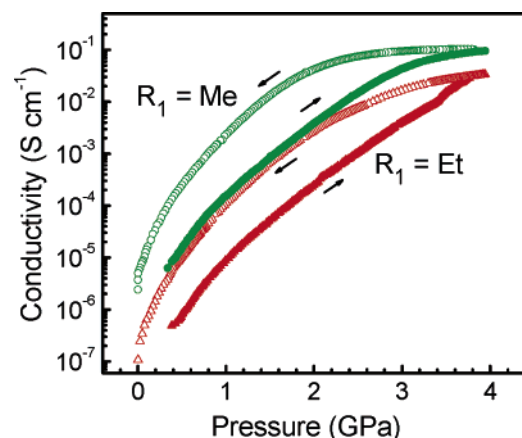


**Figure 11.** Pressure dependence of conductivity of  $[2]_2$  ( $R_1 = \text{Me}, \text{Et}; R_2 = \text{H}$ ) at 22 °C. Arrows denote direction of pressure change.

agreement with those obtained from the optical measurements, and indeed those predicted by the LMTO calculations.

At this point the analysis of these materials could be considered complete, as their structures and transport properties are self-consistent and easily rationalized. However, at the outset of our work on these systems we were intrigued by an apparent discrepancy between their conductivities as measured under controlled ambient pressure conditions and values obtained using a simple two-pin anvil system<sup>29</sup> in which the samples were compressed between two poles. Conductivity enhancements of 2 orders of magnitude could be achieved simply by hand-tightening the poles of the anvil. To explore this apparent anomaly we carried out a series of high-pressure (0.3–5.5 GPa) conductivity measurements on  $[2]_2$  ( $R_1 = \text{Me}, \text{Et}; R_2 = \text{H}$ ). These experiments revealed a dramatic pressure dependence of the conductivity of both compounds.

As illustrated in Figure 11, the room temperature conductivities show an increase with pressure of approximately 5 orders of magnitude over a 4 GPa pressure range. In accord with the ambient pressure measurements the methyl derivative has a consistently higher conductivity than the ethyl compound at all pressures. By about 4 GPa the values of  $\sigma$  (295 K) reach values near  $10^{-1} \text{ S cm}^{-1}$  ( $R_1 = \text{Me}$ ) and  $10^{-2} \text{ S cm}^{-1}$  ( $R_1 = \text{Et}$ ). Conductivity plots from both samples exhibit a significant hysteresis upon the release of pressure, but the traces for the

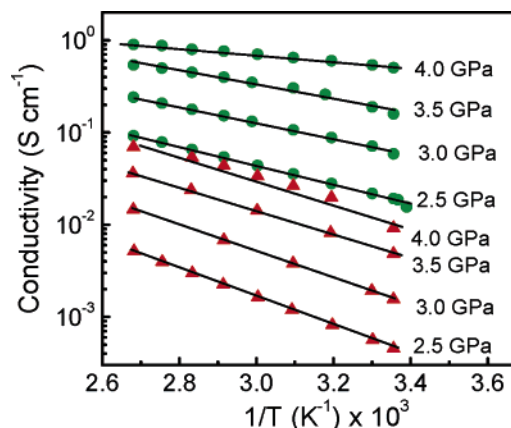


**Figure 12.** Representative log conductivity vs  $1/T$  plots for  $[2]_2$  at different pressures.  $R_1 = \text{Me}$  (circles),  $R_1 = \text{Et}$  (triangles).

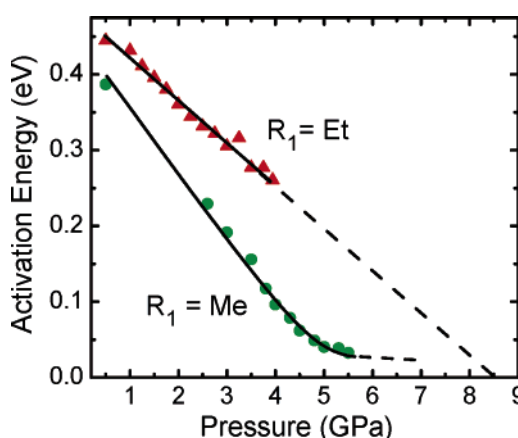


**Figure 13.** Thermal activation energies  $E_a$  of  $[2]_2$  as a function of pressure.  $R_1 = \text{Me}$  (circles),  $R_1 = \text{Et}$  (triangles).

decompression/compression data appear to converge in the low-pressure region.

Examination of the temperature dependence (from 20 to 100 °C) of the conductivity of both compounds indicates that the conductivity remains activated over the entire pressure range studied. Representative plots of log conductivity vs inverse temperature, from which activation energies  $E_a$  were derived, are shown in Figure 12. The pressure dependence of the activation energy, shown in Figure 13, is negative for both  $R_1 = \text{Me}$  ( $dE_a/dP = -5.55 \times 10^{-1} \text{ eV/GPa}$ ) and  $R_1 = \text{Et}$  ( $dE_a/dP = -5.60 \times 10^{-2} \text{ eV/GPa}$ ). While  $dE_a/dP$  for  $R_1 = \text{Me}$  is approximately an order of magnitude larger than for  $R_1 = \text{Et}$  in the pressure range up to ~4 GPa,  $dE_a/dP$  for  $R_1 = \text{Me}$  begins to decrease rapidly at higher pressure and suggests an asymptotic approach to zero  $E_a$ , i.e., the metallic state. A linear extrapolation of the  $E_a$  trend for  $R_1 = \text{Et}$  suggests metallization would be reached at ~8.5 GPa.

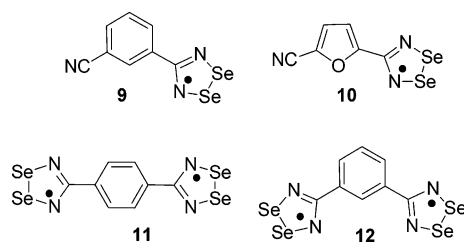
## Discussion

Improvements in the performance of neutral radical conductors require the development of materials that combine a low on-site Coulombic repulsion  $U$  with enhanced intermolecular overlap  $W$ . Within this context the bis-1,2,3-thiaselenazolyis **2** ( $R_1 = \text{Me}, \text{Et}; R_2 = \text{H}$ ) described here represent a major step forward, as the incorporation of a larger chalcogen into the highly delocalized spin distribution of the bis-1,2,3-dithiazolyl framework **1** addresses both the bandwidth and correlation

(29) Wudl, F.; Bryce, M. R. *J. Chem. Educ.* **1990**, 67, 714.



Chart 2



challenges. However, in contrast to the purely sulfur-based radicals **1** ( $R_1 = \text{Me}$ ,  $\text{Et}$ ;  $R_2 = \text{H}$ ), the selenium-containing variants **2** do not remain as radicals in the solid state. Instead they associate laterally into the Se–Se  $\sigma$ -bonded dimers  $[\mathbf{2}]_2$ , which are closed-shell materials that behave as conventional small band gap semiconductors with room-temperature conductivities near  $10^{-6} \text{ S cm}^{-1}$ .

What is striking about the bis-1,2,3-thiaselenazoyl dimers  $[\mathbf{2}]_2$ , indeed what sets them apart from other single-molecule materials, is the enhancement in their conductivity brought about by the application of relatively low external pressures. At the limit of the present experimental configuration (5.5 GPa) the conductivities of both the methyl and ethyl compounds remain thermally activated, but the activation energies are low ( $\sim 0.03 \text{ eV}$  for  $R_1 = \text{Me}$ ). To date the observation of full metallization in single-component organic crystals<sup>30</sup> has been largely restricted to iodine-containing aromatics, e.g., *p*-diiodobenzene,<sup>31</sup> hexaiodobenzene,<sup>32</sup> iodonil.<sup>33</sup> Onset of the metallic state for these systems typically requires pressures in excess of 30 GPa, i.e., far greater than those employed here. For the iodine-based compounds, bond dissociation to afford domains of metallic iodine has been proposed, although the possibility of band edge overlap has also been suggested.<sup>34</sup> The behavior we observe for  $[\mathbf{2}]_2$  is, we believe, the result of a diminution and near closure of the band gap rather than decomposition. At present we have no evidence to the contrary; samples recovered from pressure measurements display perfect infrared signatures. Moreover, neither sulfur or selenium, the two potential decomposition products, display appreciable conductivities under these pressure conditions.<sup>35,36</sup>

If the pressure response of  $[\mathbf{2}]_2$  is a result of a band gap closure, the question arises as to why the pressure effect has not been observed in other selenium-based radical dimers, notably those derived from diselenadiazoyl radicals. Previous

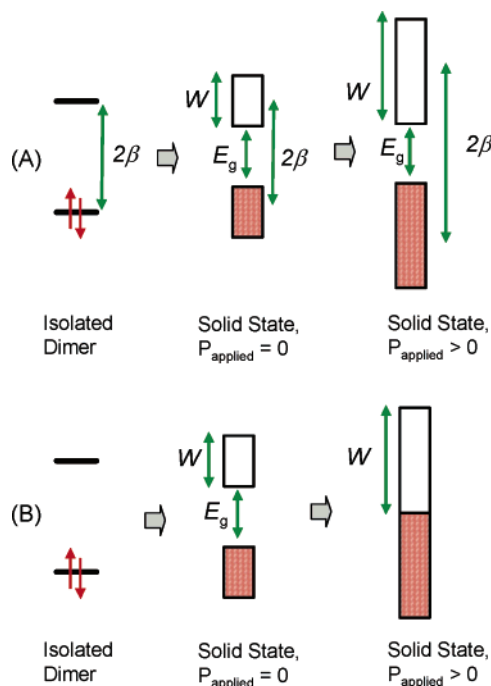


**Figure 14.** Effect of pressure on valence and conduction band splitting ( $2\beta$ ) and spreading ( $W$ ) in  $[\mathbf{8}]_2$  (A) and  $[\mathbf{2}]_2$  (B).

studies on the structures of radicals **9**–**12** (Chart 2) have revealed cofacial  $\pi$ -dimers of the type  $[\mathbf{8}]_2$  (Figure 6).<sup>20a,b,37,38</sup> Dimer dissociation energies are high, and the bulk materials remain diamagnetic to temperatures well above  $100^\circ\text{C}$ . Like  $[\mathbf{2}]_2$  they behave as intrinsic semiconductors, with room-temperature conductivities  $\sigma_{\text{RT}}$  ranging from  $10^{-9}$  to  $10^{-4} \text{ S cm}^{-1}$ , and derived band gaps  $E_g$  reaching values as low as  $0.55 \text{ eV}$  for  $[\mathbf{12}]_2$ . Compounds  $[\mathbf{10}]_2$ ,  $[\mathbf{11}]_2$ , and  $[\mathbf{12}]_2$  all show improvements in conductivity with applied pressure, but the effect is limited. In the case of  $[\mathbf{10}]_2$ , for example, the enhancement in  $\sigma$  is less than an order of magnitude at 1 GPa, with very little change in activation energy. This behavior is in marked contrast to the dramatic pressure dependence of conductivity and activation energy found in the present systems.

We attribute the dichotomy between diselenadiazoyl dimers and those described here to electronic factors arising from the different modes of association, i.e., cofacial  $\pi$  versus lateral  $\sigma$ , found in the two systems. The relatively small effect of pressure on diselenadiazoyl dimers  $[\mathbf{8}]_2$  can be understood in terms of the competing influences of intra- and interdimer orbital interactions.<sup>39</sup> On one hand an increase in pressure will enhance intermolecular overlap and hence increase the bandwidth  $W$  of both the valence and conduction bands. By itself this effect would lead to a diminution in band gap  $E_g$  (Figure 14 A). At the same time, however, compression of the dimer increases the intradimer resonance interaction  $\beta$  (Figure 6) which, in turn, will cause an increased splitting of the valence and conduction band. This intradimer effect essentially offsets the bandwidth enhancement arising from increased interdimer interactions, so that overall the change in the magnitude of band gap  $E_g$  is

- (30) Pressure effects on conductivity have been noted in two-component organic conductors. See, for example, Hutchison, K. A.; Srdanov, G.; Menon, R.; Gabriel, J.-C. P.; Knight, B.; Wudl, F. *J. Am. Chem. Soc.* **1996**, *118*, 13081.  
 (31) Brillante, A.; Della Valle, R. G.; Farina, L.; Venutti, E.; Cavazzoni, C.; Emerson, A. P. J.; Syassen, K. *J. Am. Chem. Soc.* **2005**, *127*, 3038.  
 (32) (a) Nakayama, A.; Aoki, K.; Carlön, R. P. *Phys. Rev. B: Condens. Matter* **2001**, *64*, 064104. (b) Nakayama, A.; Fujihisa, H.; Takemura, K.; Aoki, K.; Carlön, R. P. *Synth. Met.* **2001**, *120*, 767. (c) Iwasaki, E.; Shimizu, K.; Amaya, K.; Nakayama, A.; Aoki, K.; Carlön, R. P. *Synth. Met.* **2001**, *120*, 1003.  
 (33) (a) Nakayama, A.; Fujihisa, H.; Aoki, K.; Shirotani, I. *Synth. Met.* **1999**, *103*, 1901. (b) Nakayama, A.; Aoki, K.; Matsushita, Y.; Shirotani, I. *Solid State Commun.* **1999**, *110*, 627. (c) Shirotani, I.; Hayashi, J.; Yakushi, K.; Takeda, K.; Yokota, T.; Shimizu, K.; Amaya, K.; Nakayama, A.; Aoki, K. *Physica B* **2001**, *304*, 6.  
 (34) Tateyama, Y.; Ohno, T. *J. Phys.: Condens. Matter* **2002**, *14*, 10429.  
 (35) Selenium enters a semiconducting phase above 15 GPa, which transforms to a metallic phase near 25 GPa. See (a) Riggelman, B. M.; Drickamer, H. G. *J. Chem. Phys.* **1962**, *37*, 446. (b) Bundy, F. P.; Dunn, K. J. *J. Chem. Phys.* **1979**, *71*, 1550.  
 (36) Sulfur is converted to a metallic state at pressures above 40 GPa. See (a) Chhabildas, L. C.; Ruoff, A. L. *J. Chem. Phys.* **1977**, *66*, 983. (b) Dunn, K. J.; Bundy, F. P. *J. Chem. Phys.* **1977**, *67*, 5048. (c) Peanasky, M. J.; Jurgensen, C. W.; Drickamer, H. G. *J. Chem. Phys.* **1984**, *81*, 6407.

- (37) (a) Andrews, M. P. et al. *J. Am. Chem. Soc.* **1991**, *113*, 3559. (b) Cordes, A. W.; Haddon, R. C.; Hicks, R. G.; Oakley, R. T.; Palstra, T. T. M.; Schneemeyer, L. F.; Waszczak, J. V. *J. Am. Chem. Soc.* **1992**, *114*, 1729.  
 (38) Britten, J. F.; Clements, O. P.; Cordes, A. W.; Haddon, R. C.; Oakley, R. T.; Richardson, J. F. *Inorg. Chem.* **2001**, *40*, 6820.  
 (39) Beer, L.; Britten, J. F.; Cordes, A. W.; Clements, O. P.; Oakley, R. T.; Pink, M.; Reed, R. W. *Inorg. Chem.* **2001**, *40*, 4705.

smaller than would be predicted on the basis of intermolecular effects alone.

By contrast, the frontier orbital manifold for the  $\sigma$ -dimers  $[2]_2$  (Figure 7) is such that the HOMO and LUMO are not bonding and antibonding combinations arising from a  $\pi$ -SOMO/ $\pi$ -SOMO interaction. Hence, the HOMO–LUMO splitting is not directly dependent on pressure, as there is no resonance interaction  $\beta$  that couples the two orbitals. Valence and conduction band spreading, i.e., an increase in  $W$ , thus becomes the dominant consequence of applied pressure (Figure 14 B). The preexisting *chemical* pressure in  $[2]_2$ , which leads to substantial bandwidth  $W$  even at ambient pressure, requires relatively little additional *physical* pressure to increase  $W$  and close the band gap almost entirely. Eventually, however,  $\sigma$ -compression energies reassert their importance. For example,  $dE_a/dP$  for  $R_1 = \text{Me}$  begins to decrease rapidly above 4 GPa, and suggests an asymptotic approach to zero  $E_a$ , i.e., the metallic state.

## Summary and Conclusions

Bis-1,2,3-thiaselenazolyis **2** represent a new class of resonance-stabilized radicals. Their computed gas-phase ion energetics ( $\Delta H_{\text{disp}}$ ) suggest a low on-site Coulombic repulsion barrier  $U$ , and the incorporation of selenium in place of sulfur allows for enhanced intermolecular interactions and an improved bandwidth  $W$ . Taken together the high  $W/U$  ratio for these systems augurs well for their use in the design of single-component molecular conductors. The two radicals described here ( $R_1 = \text{Me}$ , Et;  $R_2 = \text{H}$ ) dimerize in the solid state in an unprecedented manner to afford Se–Se  $\sigma$ -bonded dimers  $[2]_2$ . The bulk materials are diamagnetic and behave as small band gap semiconductors. In contrast to semiconductors based on  $\pi$ -dimerized radicals, these  $\sigma$ -dimers are extremely responsive to applied pressure. Whether full metallization of these materials can be achieved at more elevated pressures remains to be seen. Continued exploration of this family of selenium-based radicals should afford materials displaying additional improvements in conductivity, both with and without applied pressure.

## Experimental Section

**General Procedures and Starting Materials.** The reagents 2,6-diaminopyridine, acetic anhydride, gallium trichloride, silver hexafluoroantimonate, methyl triflate (trifluoromethanesulfonate), sodium sulfide nonahydrate, triethyloxonium hexafluorophosphate, tetrabutylammonium tetrafluoroborate and hexate, Proton Sponge, decamethyl- and octamethylferrocene (DMFc and OMFc), selenium and selenium dioxide were obtained commercially (all from Aldrich) and used as received. Chlorine gas (reagent grade, Matheson) was also used as received, and selenium tetrachloride was prepared by direct chlorination of selenium.<sup>40</sup> 2,6-Diamino-pyridine-3,5-bis(thiocyanate) **5** was prepared as described previously.<sup>41</sup> All solvents were of at least reagent grade; acetonitrile (MeCN), dichloromethane (DCM), and dichloroethane (DCE) were dried by distillation from  $\text{P}_2\text{O}_5$  and/or CaH<sub>2</sub>. All reactions were performed under an atmosphere of dry nitrogen. Melting points are uncorrected. Infrared spectra (Nujol mulls, KBr optics) were recorded on a Nicolet Avatar FTIR spectrometer (at 2 cm<sup>−1</sup> resolution), and visible spectra were collected using a Beckman DU 640 spectrophotometer. <sup>1</sup>H NMR spectra were run on a Bruker Avance 300 MHz

NMR spectrometer. Elemental analyses were performed by MHW Laboratories, Phoenix, AZ 85018.

**Preparation of 2,6-Diaminopyridine-3,5-bis(thioacetate) 6.** 2,6-Diaminopyridine-3,5-bis(thiocyanate) (13.8 g, 0.062 mol) and sodium sulfide nonahydrate (59.5 g, 0.248 mol) were added to a degassed solution of sodium hydroxide (13.0 g, 0.325 mol) in 300 mL of water. The reaction was warmed for 1 h to afford a yellow solution, then cooled on ice and acetic anhydride slowly added to a pH of 6. The mixture was left undisturbed for 1 h, and the yellow precipitate of **6** was collected by filtration, washed with 2 × 100 mL of water, 1 × 50 mL of cold methanol, and dried in air; yield 14.0 g (0.054 mol, 88%). The product was recrystallized from 150 mL of ethanol to afford yellow crystals; yield 11.2 g (0.044 mol, 80% from crude); mp 125–126 °C. IR: 3474 (vs), 3375 (vs), 1870 (vw), 1695 (vs), 1660 (vw), 1604 (vs), 1562 (m), 1540 (s), 1456 (vs), 1377 (m), 1357 (m), 1329 (vw), 1310 (w), 1250 (w), 1136 (m), 1123 (m), 1029 (w), 1008 (w), 954 (m), 938 (s), 762 (s), 722 (vw), 628 (s), 571 (w), 531 (m), 499 (m), 440 (w), 408 (w) cm<sup>−1</sup>. <sup>1</sup>H NMR ( $\delta$ , CDCl<sub>3</sub>): 7.29 (s, 1H, aromatic), 4.92 (s, 4H, amino), 2.37 (s, 6H, methyl). Anal. Calcd for C<sub>9</sub>H<sub>11</sub>N<sub>3</sub>O<sub>2</sub>S<sub>2</sub>: C, 42.01; H, 4.31; N, 16.33%. Found: C, 42.02; H, 4.64; N, 16.09%.

**Preparation of 4*H*-Bis[1,2,3]thiaselenazolo[4,5-*b*:5',4'-*e*]pyridin-2-ium Chloride and Tetrachlorogallate [2][X] (X<sup>−</sup> = Cl<sup>−</sup>, GaCl<sub>4</sub><sup>−</sup>, R<sub>1</sub> = R<sub>2</sub> = H).** A slurry of selenium tetrachloride (1.00 g, 4.53 mmol) and selenium dioxide (0.474 g, 4.27 mmol) in 50 mL of MeCN was gently warmed for 30 min, until all solids dissolved. Selenium tetrachloride (1.00 g, 4.53 mmol) and selenium (0.34 g, 4.31 mmol) were then added to afford a brown solution. A solution of **6** (2.01 g, 7.83 mmol) in 90 mL of MeCN was added dropwise over 1 h to afford a deep-red solution and precipitate. The mixture was cooled to 0 °C, and triethylamine (3.6 mL, 25.8 mmol) was added dropwise. The reaction was then left to stir for 24 h, after which the black precipitate of crude [2][Cl] (R<sub>1</sub> = R<sub>2</sub> = H) was collected by filtration, washed with 2 × 100 mL of acetonitrile, and dried in vacuo; crude yield 2.94 g. Gallium trichloride (1.81 g, 10.3 mmol) was then added to a slurry of crude [2][Cl] (R<sub>1</sub> = R<sub>2</sub> = H) (2.94 g, 8.13 mmol) in 200 mL of acetonitrile, to afford a deep emerald-green solution. The solvent was removed by flash distillation, and the resulting [2][GaCl<sub>4</sub>] (R<sub>1</sub> = R<sub>2</sub> = H), a deep-red microcrystalline solid, was washed with 100 mL of HOAc, collected by filtration, and dried in vacuo; yield: 2.63 g (4.90 mmol, 60%). IR: 3182 (w), 1357(vs), 1253 (w), 1038 (2), 866 (w), 721 (w), 707 (m), 695 (s), 638 (m), 547 (s), 455 (m) cm<sup>−1</sup>. To reprecipitate pure [2][Cl] (R<sub>1</sub> = R<sub>2</sub> = H) pyridine was added to a solution of the tetrachlorogallate in MeCN until the color was bleached from the solution. The solid was collected by filtration, washed with 100 mL of acetonitrile, and dried in vacuo; yield 1.7 g (4.90 mmol, 100% from [2][GaCl<sub>4</sub>] (R<sub>1</sub> = R<sub>2</sub> = H)); mp > 250 °C dec. IR: 1467 (vs), 1377 (w), 1355 (vs), 1259 (w), 1040 (m), 801 (vw), 748 (vw), 720 (w), 707 (m), 689 (vw), 683 (vw), 632 (m), 531 (m), 457 (m), 408 (w) cm<sup>−1</sup>.

**Preparation of 4*H*-Bis[1,2,3]thiaselenazolo[4,5-*b*:5',4'-*e*]pyridin-2-ium Triflate [2][OTf] (R<sub>1</sub> = R<sub>2</sub> = H).** Tetrabutylammonium triflate (1.00 g, 2.56 mmol) was added to a solution of [2][GaCl<sub>4</sub>] (R<sub>1</sub> = R<sub>2</sub> = H) (1.03 g, 1.92 mmol) in 50 mL of MeCN. The solution changed color from turquoise to pale blue, and a microcrystalline red-brown precipitate formed immediately. After 30 min the product [2][OTf] (R<sub>1</sub> = R<sub>2</sub> = H) was collected by filtration, washed with 2 × 30 mL of acetonitrile, and dried in vacuo; yield 763 mg (1.61 mmol, 84%). mp > 250 °C dec. IR: 3200 (w), 1377 (w), 1238 (s br), 1166 (m), 1034 (s), 708 (s), 638 (s), 578 (w), 529 (s), 513 (w), 450 (m) cm<sup>−1</sup>.

**Preparation of 4*H*-Bis[1,2,3]thiaselenazolo[4,5-*b*:5',4'-*e*]pyridin-2-ium Hexafluoroantimonate [2][SbF<sub>6</sub>] (R<sub>1</sub> = R<sub>2</sub> = H).** Reprecipitated [2][Cl] (R<sub>1</sub> = R<sub>2</sub> = H) (4.51 g, 12.4 mmol) and AgSbF<sub>6</sub> (5.58 g, 16.2 mmol) were stirred at gentle reflux in 120 mL of MeCN for 24 h to afford a deep turquoise solution, a fine white AgCl precipitate, and a small amount of a very fine precipitate of red selenium. The solution was carefully filtered under an inert atmosphere using a glass frit of E

(40) Brauer, G. *Handbook of Preparative Inorganic Chemistry* Academic Press: New York 1963; Vol. 1, p 423.

(41) (a) Baker, A. J.; Hill, S. A. *J. Chem. Soc.* **1962**, 3464. (b) Lochon, P.; Méheux, P.; Néel J. *Bull. Soc. Chim. Fr.* **1967**, 11, 4387. (c) Okada M., Marvel, C. S. *J. Polym. Sci., Pt A-1* **1968**, 6, 1259.

porosity to remove the solids. The solvent was removed from the filtrate by flash distillation and the remaining golden microcrystalline solid dried in vacuo. The solid was washed with 50 mL of acetic acid, collected by filtration, and dried in air; yield 3.57 g (6.36 mmol, 51%); mp > 240 °C dec. Recrystallization from MeCN afforded small golden plates, which were characterized by X-ray crystallography. IR: 3317 (w), 1566 (vw), 1542 (w), 1465 (vs), 1377 (m), 1355 (s), 1244 (w), 1035 (s), 876 (vw), 739 (w), 726 (m), 711 (s), 656 (vs), 637 (m), 531 (s), 485 (vw), 454 (s), 409 (w) cm<sup>-1</sup>.

**Preparation of Bis[1,2,3]thiaselenazolo[4,5-*b*:5',4'-*e*]pyridine 7.** A solution of Proton Sponge (0.90 g, 4.20 mmol) in 10 mL of acetonitrile was added dropwise to a stirred solution of [2][SbF<sub>6</sub>] (R<sub>2</sub> = R<sub>1</sub> = H) (2.02 g, 3.49 mmol) in 40 mL of acetonitrile. The solution changed color from turquoise to pale pink, and a dark-gray precipitate formed immediately. After 10 min the product **7** was collected by filtration, washed with 2 × 30 mL of acetonitrile, and dried in vacuo; yield 1.13 g (3.48 mmol, 100%); mp > 150 °C dec. IR: 1481 (vs), 1466 (s), 1370 (s), 1331 (m), 1270 (vw), 1096 (m), 1033 (s), 853 (m), 742 (m), 737 (m), 723 (w), 694 (vw), 686 (s), 530 (m), 453 (w), 441 (vw), 434 (vw) cm<sup>-1</sup>. The product could not be recrystallized due to its insolubility in organic media.

**Preparation of 4-Methyl-4*H*-bis[1,2,3]thiaselenazolo[4,5-*b*:5',4'-*e*]pyridin-2-ium Triflate [2][OTf] (R<sub>1</sub> = Me, R<sub>2</sub> = H).** Methyl triflate (1.58 g, 9.64 mmol) and Proton Sponge (685 mg, 3.21 mmol) were added to a slurry of **7** (1.05 g, 3.21 mmol) in 30 mL of DCE, and the mixture stirred at room temperature for 24 h. The red, microcrystalline solid was collected by filtration, washed with 20 mL of DCE, and dried in vacuo; yield 1.42 g (2.9 mmol, 90%). Recrystallization from hot MeCN afforded red, lustrous plates of [2][OTf] (R<sub>1</sub> = Me, R<sub>2</sub> = H), mp > 240 °C dec. UV-vis (DCM) λ<sub>max</sub>: 683 nm (log ε = 4.6). IR: 1713 (m), 1484 (s), 1462 (vs), 1377 (s), 1362 (s), 1305 (vw), 1270 (s), 1236 (s), 1224 (m), 1166 (w), 1140 (vw), 1024 (s), 954 (vw), 857 (vw), 760 (vw), 739 (vw), 723 (w), 704 (m), 637 (s), 586 (m), 517 (w), 459 (w) cm<sup>-1</sup>. <sup>1</sup>H NMR (δ CD<sub>3</sub>CN): 7.80 (s, 1H, aromatic), 3.67 (s, 3H, methyl). Anal. Calcd for C<sub>7</sub>H<sub>4</sub>F<sub>3</sub>N<sub>3</sub>O<sub>3</sub>S<sub>2</sub>Se<sub>2</sub>: C, 17.18; H, 0.82; N, 8.59%. Found: C, 17.44; H, 1.22; N, 8.90%.

**Preparation of 4-Ethyl-4*H*-bis[1,2,3]thiaselenazolo[4,5-*b*:5',4'-*e*]pyridin-2-ium Tetrafluoroborate [2][BF<sub>4</sub>] (R<sub>1</sub> = Et, R<sub>2</sub> = H).** Triethyloxonium hexafluorophosphate (1.24 g, 5.00 mmol) and Proton Sponge (355 mg, 1.66 mmol) were added to a slurry of **7** (540 mg, 1.66 mmol) in 30 mL of DCE, and the mixture stirred at room temperature for 24 h. The red, microcrystalline solid was collected by filtration, washed with 20 mL of DCE, and dried in vacuo, crude yield 830 mg (100%). The crude [2][PF<sub>6</sub>] (R<sub>1</sub> = Et, R<sub>2</sub> = H) was dissolved in 20 mL of THF and the solution carefully filtered through a glass frit of E porosity. Tetrabutylammonium tetrafluoroborate (0.715 mg, 2.17 mmol) was added to the filtrate, and the solvent was removed by flash distillation. The resulting red microcrystalline solid was washed with DCE, collected by filtration, and dried in vacuo, yield 287 mg (0.65 mmol, 54%). Recrystallization from hot MeCN afforded lustrous, red plates of [2][BF<sub>4</sub>] (R<sub>1</sub> = Et, R<sub>2</sub> = H), mp > 240 °C dec. UV-vis (DCM) λ<sub>max</sub>: 682 nm (log ε = 4.6). IR: 31974 (vw), 1407 (vw), 1355 (s), 1264 (s), 1238 (vs), 1166 (s), 1034 (vs), 889 (w), 830 (vw), 760 (m), 709 (vs), 668 (s), 628 (s), 579 (m), 518 (m), 513 (s), 450 (vs), 405 (m) cm<sup>-1</sup>. <sup>1</sup>H NMR (CD<sub>3</sub>CN): 7.80 (s, 1H, aromatic), 4.25 (q, 7.1 Hz, CH<sub>2</sub>), 1.28 (tr, 7.1 Hz, CH<sub>3</sub>). Anal. Calcd for C<sub>7</sub>H<sub>6</sub>BF<sub>4</sub>N<sub>3</sub>S<sub>2</sub>Se<sub>2</sub>: C, 19.06; H, 1.37; N, 9.53%. Found: C, 19.31; H, 1.16; N, 9.60%.

**Preparation of 4-Methyl- and 4-Ethyl-4*H*-bis[1,2,3]thiaselenazolo[4,5-*b*:5',4'-*e*]pyridin-3-yl [2]<sub>2</sub> (R<sub>1</sub> = Me, Et; R<sub>2</sub> = H).** Crystals of [2]<sub>2</sub> (R<sub>1</sub> = Me, Et; R<sub>2</sub> = H) suitable for X-ray work were grown by slow diffusion of degassed solutions (five freeze-pump-thaw cycles) of [2][OTf] (R<sub>1</sub> = Me, R<sub>2</sub> = H) or [2][BF<sub>4</sub>] (R<sub>1</sub> = Et, R<sub>2</sub> = H) (typically 20–40 mg) in ca. 15 mL of MeCN into solutions of OMFc (typically 20–40 mg) in ca. 10 mL of MeCN at 0 °C. Small, burnished gold needles of radical formed almost immediately at the interface and were harvested after 12–16 h. R<sub>1</sub> = Me: IR: 1486 (m), 1314 (s), 1174 (w),

1011 (m), 848 (w), 715 (w), 699 (s), 656 (w) 561 (m), 506 (w), 449 (w), 431 (w) cm<sup>-1</sup>. Anal. Calcd for C<sub>6</sub>H<sub>4</sub>N<sub>3</sub>S<sub>2</sub>Se<sub>2</sub>: C, 21.18; H, 1.19; N, 12.35%. Found: C, 21.58; H, 0.86; N, 12.56%. R<sub>1</sub> = Et: IR: 1359 (m), 1337 (m), 131 (w), 1286 (m), 1164 (m), 1035 (m), 855 (m), 717 (m), 696 (s), 677 (w), 655 (m), 562 (m), 451 (m), 403 (m) cm<sup>-1</sup>. Anal. Calcd for C<sub>7</sub>H<sub>6</sub>N<sub>3</sub>S<sub>2</sub>Se<sub>2</sub>: C, 23.74; H, 1.71; N, 11.86%. Found: C, 23.90; H, 1.51; N, 12.10%.

**Cyclic Voltammetry.** Cyclic voltammetry was performed using a PINE Bipotentiostat, model AFCCIBP1, with scan rates of 50–100 mV s<sup>-1</sup> on solutions (<10<sup>-3</sup> M) of [2][OTf] (R<sub>1</sub> = Me) and [2][BF<sub>4</sub>] (R<sub>1</sub> = Et) in oxygen-free MeCN (dried by distillation from CaH<sub>2</sub>) containing 0.1 M tetra-*n*-butylammonium hexafluorophosphate. Potentials were scanned with respect to the quasi-reference electrode in a single compartment cell fitted with Pt electrodes and referenced to the Fc/Fc<sup>+</sup> couple of ferrocene at 0.38 V vs SCE.<sup>42</sup> The E<sub>pa</sub>–E<sub>pc</sub> separation of the reversible couple was within 10% of that of the Fc/Fc<sup>+</sup> couple.

**EPR Spectra.** X-Band EPR spectra were recorded at ambient temperature using a Bruker EMX-200 spectrometer; a sample of **2** (R<sub>1</sub> = Et, R<sub>2</sub> = H) was generated by dissolving the dimer [2]<sub>2</sub> (R<sub>1</sub> = Et, R<sub>2</sub> = H) in degassed dichloromethane. Hyperfine coupling constants were obtained by spectral simulation using Simfonia.<sup>43</sup>

**X-ray Measurements.** Samples for analysis were glued to a glass fiber with epoxy. X-ray data were collected at 293 and 95 K with a Bruker SMART APEX CCD-based diffractometer using ω-scans. Intensity decay over the course of the data collections was evaluated by re-collecting the first 50 frames of data at the end of the experiment; no significant decay was noted. The reflection data were processed using SAINT.<sup>44</sup> The structures were solved by direct methods using SHELXS-90<sup>45</sup> and refined by least-squares methods on F<sup>2</sup> using SHELXL-97<sup>46</sup> incorporated in the SHELXTL<sup>47</sup> suite of programs. All non-hydrogen atoms were refined anisotropically; hydrogen atoms were located on difference maps and refined isotropically. Details of data collection and refinement are presented in Table 3.

**Magnetic Susceptibility Measurements.** Magnetic susceptibility measurements were performed over the temperature range 5–350 K on a George Associates Faraday balance operating at 0.5 T.

**Ambient Pressure Conductivity Measurements.** Ambient pressure single-crystal (needle axis) conductivity measurements on [2]<sub>2</sub> (R<sub>1</sub> = Et, R<sub>2</sub> = H) were made using a four-probe configuration, with in-line contacts made using silver paint. Conductivity was measured in a custom-made helium variable-temperature probe using a Lake Shore 340 temperature controller. A Keithley 236 unit was used as a voltage source and current meter, and two 6517A Keithley electrometers were used to measure the voltage drop between the potential leads in the four-probe configuration. Four-probe measurements on [2]<sub>2</sub> (R<sub>1</sub> = Me, R<sub>2</sub> = H) were performed on a pressed pellet sample (with silver paint contacts) using a homemade device to determine the voltage drop.

**High-Pressure Conductivity Measurements.** The high-pressure temperature conductivity experiments were carried out in a cubic anvil press<sup>48</sup> using pyrophyllite (Al<sub>4</sub>Si<sub>8</sub>O<sub>20</sub>(OH)<sub>4</sub>) as the pressure-transmitting medium. Sample pressure was determined from previous calibrations of the applied hydraulic load against pressures of structure transformations in standards at room temperature (Hg L ↔ I at 0.75 GPa, Bi I ↔ II at 2.46 GPa, Tl I ↔ III at 3.70 GPa, and Ba I ↔ II at 5.5 GPa).<sup>49</sup> Temperature was applied by Joulean heating of a cylindrical Nb foil (0.127 mm thick) furnace and monitored with a Pt(Pt + 10% Rh)

(42) Boeré, R. T.; Moock, K. H.; Parvez, M. Z. *Anorg. Allg. Chem.* **1994**, 620, 1589.

(43) WinEPR Simfonia, Bruker Instruments, Inc., Billerica, MA.

(44) SAINT, version 6.22 Bruker Advanced X-ray Solutions, Inc., Madison, WI, 2001.

(45) Sheldrick, G. M. SHELXS-90. *Acta Crystallogr. A* **1990**, 46, 467.

(46) Sheldrick, G. M. SHELXL-97. Program for the Refinement of Crystal Structures, University of Göttingen, Göttingen, Germany, 1997.

(47) SHELXTL, VERSION 6.12 Program Library for Structure Solution and Molecular Graphics Bruker Advanced X-ray Solutions, Inc., Madison, WI, 2001.

(48) Secco, R. A. *Can. J. Phys.* **1995**, 73, 287.

(49) Secco, R. A.; Schloessin, H. H. *J. Appl. Phys.* **1986**, 60, 1625.



thermocouple, using a pressure-corrected emf.<sup>49,50</sup> Two Pt electrodes, each constructed from a single length of wire, contacted the disk-shaped ( $\sim 6.1$  mm diameter and  $\sim 0.35$  mm thick), pre-compacted, powder sample which was contained in a boron nitride ( $\sigma_{\text{BN}} \leftrightarrow 10^{-11} (\Omega \text{ cm})^{-1}$ ) cup. Both two-wire dc (Solartron 7061 Systems voltmeter) and four-wire ac (1 Hz and 1 kHz – Solartron 1260 impedance analyzer) resistance measurements were made. Separate experiments were performed at room temperature vs pressure (0.3–5.5 GPa) and at fixed pressures vs temperature (22–100 °C). In the constant room-temperature experiments, resistance was measured on increasing/decreasing pressure over 5–6 h. In the variable temperature experiments, resistance was measured at fixed temperature intervals of 10 °C on heating/cooling at constant pressure. Pressure was increased and temperature was cycled again. The contiguous disk-shaped sample was extracted from the recovered pressure cell, and the sample geometry was measured to convert resistance to conductivity. The IR spectrum of the recovered sample showed no change in comparison with the pre-compression spectrum.

**Electronic Structure Calculations.** The ion energetics data shown in Table 1 were obtained from calculations using the B3LYP method, as contained in the Gaussian 98W suite of programs.<sup>51</sup> Adiabatic ( $\Delta\text{SCF}$ ) ionization potential and electron affinity estimates were obtained from total electronic energy calculations using a 6-31G\*\* basis set within the constraints of  $C_{2v}$  symmetry. Full vibrational frequency calculations on the final geometries of the radical and cation confirmed that they were stationary points. In the case of the anions, there was one negative frequency, which may be interpreted in terms of an incipient cleavage of one of the E–E<sup>52</sup> or E–N<sup>20d</sup> (E = S, Se) bonds upon reduction of the radical. Radical association energies were

estimated in terms of the total electronic energy (B3LYP/6-31G\*\*) difference between the radicals and their dimers. Dimer geometries were optimized within a  $C_{2h}$  symmetry constraint and were confirmed to be stationary points by frequency calculations. The self-consistent tight-binding LMTO calculations (LMTO = linear muffin tin orbitals) were carried out on  $[\text{2}]_2$  ( $\text{R}_1 = \text{Me, Et}$ ;  $\text{R}_2 = \text{H}$ ) using the atomic spheres approximation (ASA).<sup>53</sup> In the LMTO approach, the density functional theory is used with the local density approximation (LDA).<sup>54</sup> Atomic positions were taken from the crystallographic data. The eigenvalue problem was solved on a set of 510 (methyl) and 460 (ethyl)  $k$  points of the irreducible wedge of the first Brillouin zone.

**Acknowledgment.** We thank the Natural Sciences and Engineering Research Council of Canada (NSERCC), the U.S. Office of Basic Energy Sciences, Department of Energy (Grant Number DEFG02-04ER46138) for financial support. We also thank the Kentucky Research Challenge Trust Fund for the purchase of CCD X-ray equipment and an X-ray facility upgrade, and the NSERC and Ontario Provincial Government for postgraduate scholarships to L.B., J.L.B., and A.A.L.

**Supporting Information Available:** Archival files for the G98 calculations and complete authorship for refs 37a and 51; details of X-ray crystallographic data collection and structure refinement, tables of atomic coordinates, bond distances and angles, anisotropic thermal parameters, and hydrogen atom positions in CIF format. This information is available free of charge via the Internet at <http://pubs.acs.org>.

JA055122B

(50) Bundy, F. P. *J. Appl. Phys.* **1961**, 32, 483.

(51) Gaussian 98, Revision A: 6. Frisch, M. J. et al. Gaussian, Inc., Pittsburgh, PA, 1998.

(52) Antonello, S.; Benassi, R.; Gavioli, G.; Taddei, F.; Maran, F. *J. Am. Chem. Soc.* **2002**, 124, 7529.

(53) (a) Andersen, O. K. *Phys. Rev.* **1975**, B12, 3060. (b) Skriver, H. L. *The LMTO Method*; Springer: Berlin, Germany, 1984.

(54) Hedin, L.; Lundqvist, B. I. *J. Phys.* **1971**, 4C, 2064.